Valley-contrasting physics in all-dielectric photonic crystals: Orbital angular momentum and topological propagation

Xiao-Dong Chen, Fu-Li Zhao, Min Chen, and Jian-Wen Dong[*]

School of Physics & State Key Laboratory of Optoelectronic Materials and Technologies, Sun Yat-sen University, Guangzhou 510275, China

The valley has been exploited as a binary degree of freedom to realize valley-selective Hall transport and circular dichroism in two-dimensional layered materials, in which valley-contrasting physics is indispensable in making the valley index an information carrier. In this Rapid Communication, we reveal valley-contrasting physics in all-dielectric valley photonic crystals. The link between the angular momentum of light and the valley state is discussed, and unidirectional excitation of the valley chiral bulk state is realized by sources carrying orbital angular momentum with proper chirality. Characterized by the nonzero valley Chern number, valley-dependent edge states and the resultant broadband robust transport is found in such an all-dielectric system. Our work has potential in the orbital angular momentum assisted light manipulation and the discovery of valley-protected topological states in nanophotonics and on-chip integration.

The valley—the energy extrema of a band structure at momentum space—is a ubiquitous discrete degree of freedom (DoF) in periodic systems. It has been employed to achieve a number of intriguing phenomena such as valley-selective Hall transport and circular dichroism in two-dimensional monolayer electronic materials [1–10], in which valley-contrasting physics is essential in making the valley index an information carrier in valleytronics [11]. It is an interesting question whether one can employ a valley DoF to explore the light manipulation in photonic systems. Recently, the valley DoF was exploited in transverse electric modes of all-Si photonic crystals with triangular-shape rods [12]. There are also other ways to employ valley DoF by constructing an asymmetric AB sublattice with circular rods that are preferred in nanofabrication. On the other hand, orbital angular momentum (OAM) is another attractive topic, inspiring the cutting-edge fields of mode-multiplexing optical communications [13–15], unidirectional light transport [16–20], and vortex states in phononic crystal [21]. Recently, pseudospin associated with angular momentum has been demonstrated as a measurable physical quantity in honeycomb photonic lattices [22]. Meanwhile, topological photonics has also attracted attention for the unprecedented opportunity in the emerging field of nontrivial states [23–29]. However, it is required for the materials with magnetism, bianisotropy, or the delicate design of diffraction optical elements. Such complexity will impede spin-orbit interaction of light in nanophotonics.

In this Rapid Commnication, we reveal valley-contrasting physics in an all-dielectric valley photonic crystal (VPC) which is a hexagonal lattice of silicon rods. Using the valley as a binary DoF, the unidirectional excitation of valley chiral bulk states is realized by sources carrying OAM with proper chirality. Nontrivial topology and phase transition are found by inspecting the nonzero valley Chern number. Valley-dependent edge states enable the suppression of intervalley scattering along the zigzag boundary, leading to valley-protected broadband robust transport in a photonic crystal waveguide bend.

As depicted in Fig. 1(a), the VPC is a composite of two interlaced triangular lattices with the same lattice constants. The unit cell consists of two silicon rods embedded in an air background, e.g., the A and B rods in the dashed rhomboid or dashed hexagon. The A rod has a diameter of $d_A = 0.5a$ while the B rod has $d_B = 0.38a$, where a is the lattice constant. The relative permittivity of each rod is $\varepsilon = 11.7$. Figure 1(b) shows the two lowest bulk bands of transverse-magnetic states with a nonzero out-of-plane component of electric fields (E_z) and nonzero in-plane component of magnetic fields ($\vec{H}_\parallel$). Due to the inversion asymmetry ($d_A \neq d_B$), the bulk states can split at the two inequivalent but time-reversal valleys (K' and K), leading to a complete band gap in the whole Brillouin zone [Fig. 1(e)]. Two pairs of valley states exist at the frequencies of 0.244 and 0.272 c/a at the K' and K points. These separated photonic valley states show chirality as they have intrinsic circular-polarized OAM, which can be verified by the phase distribution of E_z, i.e., arg(E_z). In Fig. 1(c), the E_z phase of the K' valley state decreases counterclockwise by 2π and thus has a circular OAM. To characterize the OAM term, we define topological charge as $l = \oint_L \nabla[\arg(E_z)] d\vec{s}/2\pi$, where L is a closed contour surrounding the unit cell center [30]. In this way, the E_z field has a circular OAM with $l = -1$ around the central point. In contrast, the E_z phases of the K valley state are reversed to be clockwise deceasing, and thus the E_z field has a circular OAM with $l = 1$ [Fig. 1(d)]. Note that OAM with a higher topological charge can be achieved in higher-order valley chiral states. For example, to reach $|l| = 2$, quadruple valley chiral states with higher frequencies should be considered. Note also that as correlated by Maxwell equations, the E_z field with circular $l = -1$ ($l = 1$) OAM can lead to the $\vec{H}_\parallel$ field with left-handed (right-handed) spin angular momentum (SAM) at the origin (Appendix A in the Supplemental Material [31]). Consequently, the $l = -1$ ($l = 1$) OAM can be denoted as left-handed circular polarized (LCP) and right-handed circular polarized (RCP) OAM, respectively. Note also that similar valley-contrasting physics can be found in either TM-like states (Appendix B in the Supplemental Material [31]) or TE-like states [32–34] of photonic crystal slabs.

———————
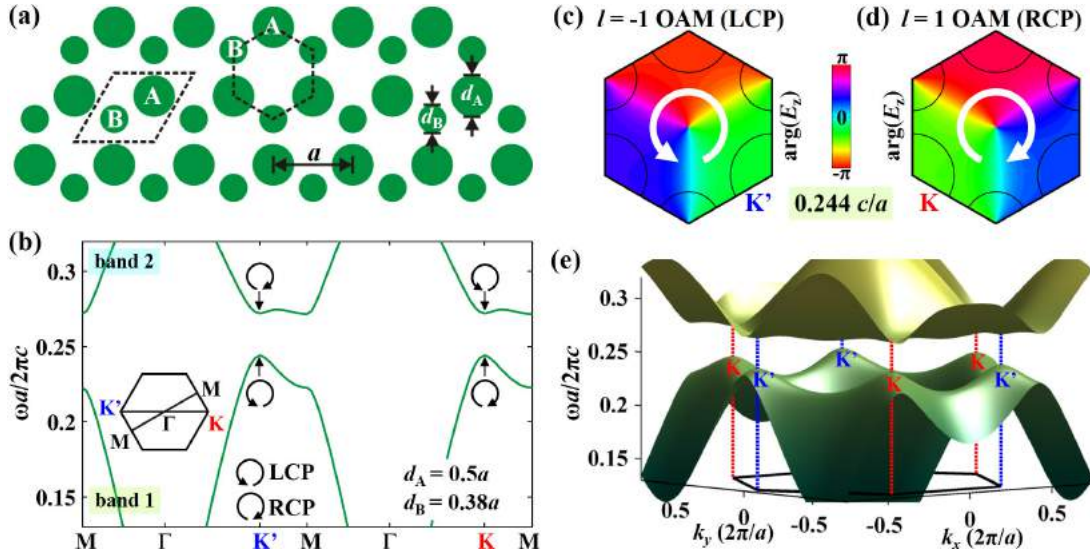[*]dongjwen@mail.sysu.edu.cn

FIG. 1. Valley-contrasting OAM in VPC. (a) Schematic of the VPC with the unit cell of two silicon rods embedded in an air background, e.g., A and B rods in the dashed rhomboid or dashed hexagon. The rod diameters are $d_A = 0.5a$ and $d_B = 0.38a$, where a is the lattice constant. (b) Two lowest bulk bands of transverse-magnetic modes, in which four valley states carrying intrinsic OAM are marked by either counterclockwise or clockwise arrows. Valley-contrasting chiral OAM and the phase distributions of E_z, i.e., $\arg(E_z)$, at the frequency of $0.244\,c/a$ at the (c) K' point and (d) K point. The phases of E_z for the K' valley state decrease counterclockwise by 2π, indicating the OAM with a topological charge of $l = -1$ and further leading to LCP spin angular momentum at the center of the unit cell. While for the K valley state, $\arg(E_z)$ decreases clockwise and has a topological charge of $l = 1$ (denoted as RCP OAM). (e) Three-dimensional bulk band structure, illustrating the complete gap and two inequivalent but time-reversal valleys.

The valley dependence of OAM chirality can be used to achieve unidirectional excitation of valley chiral states by external sources with proper chirality. In Fig. 2(a), we consider E_z line sources (yellow marker, inset) with the same magnitudes but phases carrying chiral OAM exciting around the center of the VPC with six zigzag boundaries.

The operating frequency is set to be $0.244\,c/a$. The valley chiral state will be excited only when its chirality matches the chirality of the E_z source. So when the phases of the E_z source decrease counterclockwise, i.e., LCP chirality [left panel in Fig. 2(b)], it couples to the K' valley state. At each boundary, the excited K' valley state is partly reflected
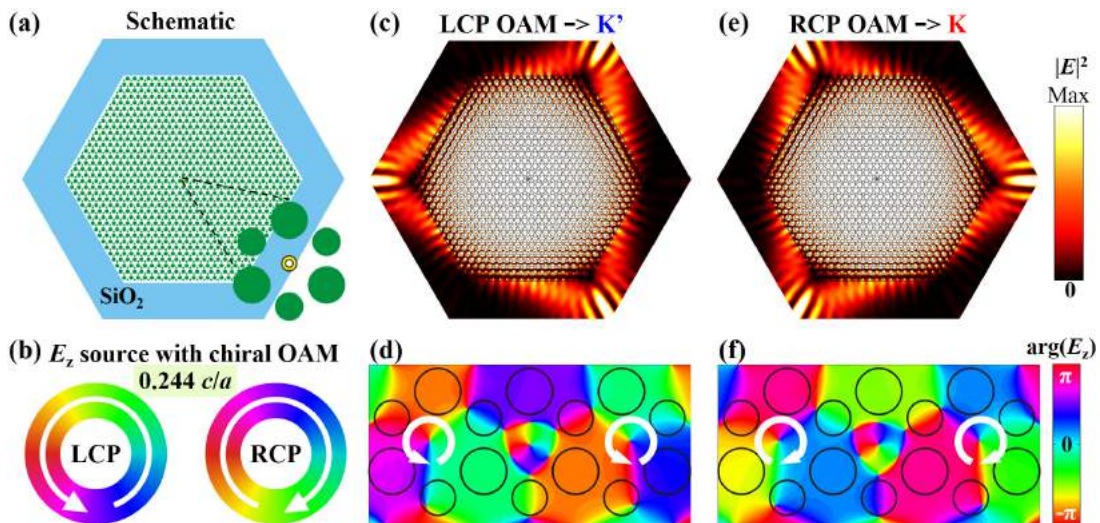

FIG. 2. Unidirectional excitation of valley chiral states by E_z source with chiral OAM. (a) Schematic of the hexagonal VPC with six zigzag boundaries, surrounded by a homogeneous SiO$_2$ medium. Inset: yellow marker indicates the circular E_z line sources around the center of the sample. (b) Schematic of the circular E_z line sources with the same magnitudes but phases carrying LCP OAM (left panel) or RCP OAM (right panel) at the frequency of $0.244\,c/a$. (c) Electric intensity and (d) E_z phases of the excited K' valley state when applying the LCP source. (e) Electric intensity and (f) E_z phases of the excited K valley state when the source chirality is RCP. Note that it is experimentally detectable for the distinct differences of refracted beam directions at each boundary and the phase distributions inside the sample, verifying the unidirectional excitation of valley chiral states.

back into the VPC and partly refracted into the surrounding SiO$_2$ medium according to the conservation of the momentum parallel to the boundary [Fig. 2(c)]. Particularly, the refracted light beams are interfered with and enhanced at the leftmost, upper-right, and lower-right corners of the sample. In Fig. 2(d), the phases of the E_z field inside the VPC show LCP chirality, confirming the excitation of the K' valley state (see detailed field distributions in Appendix C in the Supplemental Material [31]). When the phases of the E_z source have the opposite chirality, i.e., RCP chirality as shown in the right panel of Fig. 2(b), it will couple to the K valley states and the output directions are reversed to enhance at the rightmost, upper-left and lower-left corners of the sample [Fig. 2(e)], and the excited E_z phases will show RCP chirality [Fig. 2(f)]. Such distinct differences of the refracted light-beam directions and the phase distributions are experimentally detectable, and in turn prove the unidirectional excitation of valley chiral states. Note that the input sources carrying OAM can be experimentally achieved by discrete dipoles with the same amplitude but decreasing phase shift in the microwave frequency region, and can be excited by circular polarized incident light via spin-orbit conversion [34] in the near-infrared/visible frequency region. Due to the correspondence between the E_z field with chiral OAM and the $\vec{H}_\parallel$ field with circular polarized SAM (Appendix A in [the Supplemental Material [31]]), there is no doubt that the valley chiral states can be also selectively excited by an in-plane point source with chiral SAM. Note also that electromagnetic modes carrying different OAM can be used to constitute topological edge electromagnetic transportation was first proposed in C6-symmetric photonic crystals [35].

Next, we will show the nontrivial topology of this all-dielectric VPC. We construct a minimal band model of bulk dispersions and resort to the photonic effective Hamiltonian through the **k·p** approximation (see [12,26] and the Supplemental Material [31],

$$\hat{H} = v_D(\hat{\sigma}_x \hat{\tau}_z \delta k_x + \hat{\sigma}_y \delta k_y) + \lambda^P_{\varepsilon_z} \hat{\sigma}_z, \tag{1}$$

where $\vec{\delta k}$ measures from the valley center K' or K point. $\hat{\sigma}_i$ and $\hat{\tau}_i$ are the Pauli matrices acting on sublattice and valley spaces, respectively. The last term $\lambda^P_{\varepsilon_z} \hat{\sigma}_z$ opens a frequency band gap with a bandwidth of $2\lambda^P_{\varepsilon_z}$ at the valley centers due to the inversion asymmetry. Specifically, $\lambda^P_{\varepsilon_z} \propto [\int_B \varepsilon_z ds - \int_A \varepsilon_z ds]$, where $\int \varepsilon_z ds$ denotes the integration of ε_z at either the A or B rod domain. Take the VPC with $d_A = 0.5a$ and $d_B = 0.38a$ in Fig. 1 as an example; $\int_B \varepsilon_z ds < \int_A \varepsilon_z ds$ leads to $\lambda^P_{\varepsilon_z} < 0$ and thus a complete band gap clearly exists in Fig. 1(b). Moreover, the effective Hamiltonian implies a valley-dependent topological index of Berry curvature $C_{\tau_z} = \tau_z \text{sgn}(\lambda^P_{\varepsilon_z})/2$ [1,12]. Then for the VPC in Fig. 1, the topological indices at K' and K valleys are $C_{K'} = +1/2$ and $C_K = -1/2$, schematically denoted by the white "+" and "−" symbols in the right panel of Fig. 3(a). The inversion asymmetric VPC does acquire the nonzero topological invariant—valley Chern number $C_v = (C_K - C_{K'}) = -1$. Note that as each Dirac point contributes π or $-\pi$ Berry flux, the valley Chern number limits to ± 1 when just one pair of Dirac points is gapped. For a large valley Chern number, one may find multiple pairs of Dirac points along a mirror-symmetric reciprocal axis, and then lift
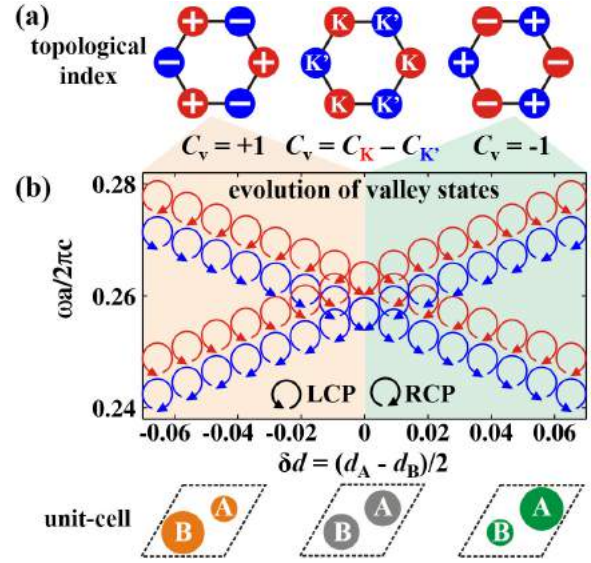

FIG. 3. Valley-dependent topological index distribution and phase transition. (a) Schematics of topological index distributions for VPC with $\delta d < 0a$ and $\delta d > 0a$. The white $+$ and $-$ symbols represent the topological index for Berry curvature with $+1/2$ and $-1/2$ in each valley, respectively. Nonzero valley Chern numbers, $C_v = (C_K - C_{K'})$, are used to distinguish the topology. (b) Frequency spectra of valley chiral states as a function of the inversion-asymmetry amplitude described by $\delta d = (d_A - d_B)/2$. When δd decreases, the frequencies are boosted for both the LCP K' valley state and the RCP K valley state, while they drop for the other two valley states. The state exchange occurs at $\delta d = 0a$, resulting in phase transition and the two topologically distinct VPCs. In (b), K' and K valley states are, respectively, represented by blue and red circular arrows, according to the OAM chirality.

the degenerate points by lowering the point-group symmetry [36,37].

As the topological index C_{τ_z} and the valley Chern number are dependent on the sign of $\lambda^P_{\varepsilon_z}$, the phase transition is expected when the sign of $\lambda^P_{\varepsilon_z}$ is flipped. Here, we alter the diameter of the two silicon rods to study different VPCs with inversion-asymmetry amplitude denoted by $\delta d = (d_A - d_B)/2$. Figure 3(b) plots the frequency spectra of valley chiral states as a function of δd, while keeping the average diameter $(d_A + d_B)/2$ unchanged. With the decrease of δd, the radius of the A rod becomes smaller while that of the B rod becomes larger [see insets at the bottom of Fig. 3(b)]. In addition, the valley frequencies of the LCP state at the K' valley and the RCP state at the K valley will boost. On the other hand, the frequencies of the other two valley chiral states, i.e., the RCP state at the K' valley and the LCP state at the K valley, will drop with the decrease of δd. The state exchange between valley states with opposite chirality occurs at the critical point of $\delta d = 0a$, causing the flipped sign of $\lambda^P_{\varepsilon_z}$ and the reversal of topological index distributions. The left panel of Fig. 3(a) illustrates that the topological index is $+1/2$ at the K valley (red) and $-1/2$ at the K' valley (blue) for the VPC with $\delta d < 0a$, resulting in a positive valley Chern number of $C_v = +1$, which is different from that of the VPC with $\delta d > 0a$. Hence the topological invariant of the valley
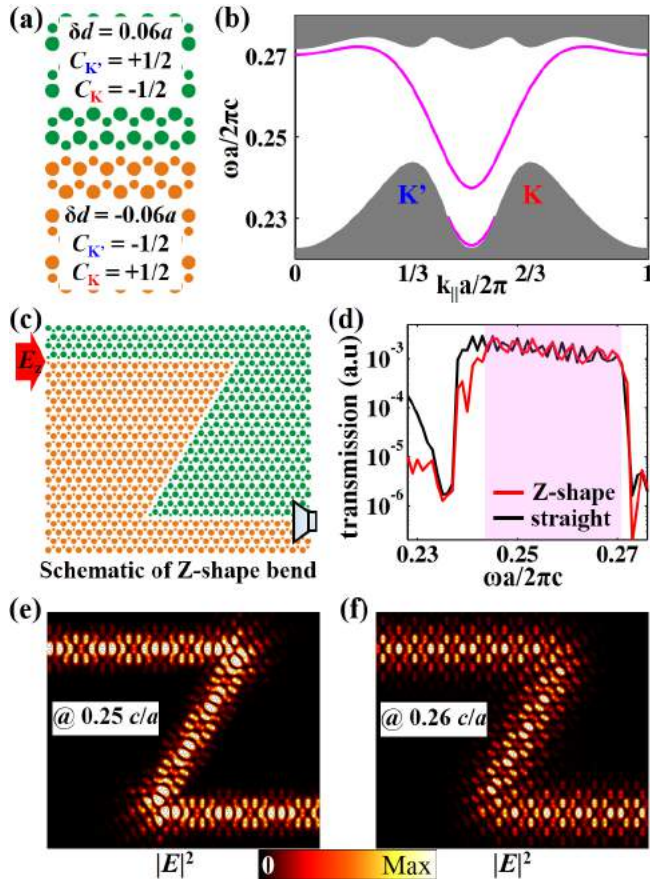
FIG. 4. Broadband robust transmission and valley-dependent edge states. (a) Schematic of the edge constructed by a VPC with $\delta d = -0.06a$ (orange) and the other with $\delta d = 0.06a$ (green). (b) Valley-dependent edge states, including one with negative velocity at the K' valley and the other with positive velocity at the K valley. (c) Schematic of the Z-shape bend, with an incident E_z source (red) and the transmission detector (gray). (d) Transmission spectra for the Z-shape bend (red) and the straight channel (black) and broadband robust transmission are found from 0.244 to 0.272 c/a. (e,f) Electric field intensity at 0.25 and 0.26 c/a, illustrating the smooth propagating waves through the Z sharp corners.

Chern number changes and the topological phase transition is well demonstrated in the VPC.

The nonzero valley Chern number shows intrinsic nontrivial topology, implying to achieve robust edge states at the boundary of two topologically distinct VPCs. Figure 4(a) shows the schematic of an edge constructed by a VPC with $\delta d = -0.06a$ at the bottom (orange) and one with $\delta d = 0.06a$ (green) at the top. Across the boundary, the topological index differences at the K' and K valleys are -1 and $+1$. It leads to the valley-dependent edge states [12], i.e., one edge state with negative velocity at the K' valley and one with positive velocity at the K valley [Fig. 4(b)]. Note that the valley-dependent edge

states *do not* have the same origin as those in photonic quantum Hall effect by breaking time-reversal symmetry [23,24], as the Chern number in the VPC is zero. This is also why the edge dispersions in Fig. 4(b) are gapped and do not connect the upper and lower bulk bands. However, they can still be employed for constructing a waveguide with broadband robust transport against sharp corners, as the intervalley scattering is suppressed due to the vanishing field overlapping between two valley states [12]. As a representative example, we construct the Z-shape bend in Fig. 4(c), and position an E_z source at the entrance and a detector at the exit. When the operating frequency is within the complete gap from 0.244 to 0.272 c/a, the wave will not suffer from backscattering even if it encounters the sharp corners. As a result, broadband robust transport is achieved, verified by the fact that the transmittance of the Z-shape bend (red) is as high as that of a straight channel (black), with a wide bandwidth of 10% [Fig. 4(d)]. The field patterns at frequencies of 0.25 and 0.26 c/a are also plotted in Figs. 4(e) and 4(f), so as to show the smooth, round-turn passing at the two corners. Such valley-protected transport of light is different from the resonance-type configuration, e.g., the standard W1 waveguide [38,39]; also see the comparison in Appendix F in the Supplemental Material [31].

In conclusion, the valley DoF has been explored to realize valley-contrasting OAM and topological chiral states inside all-dielectric VPCs. When the inversion symmetry is broken, the valley chiral states with intrinsic chiral OAM are unveiled. Unidirectional excitation of valley chiral states is achieved by sources carrying OAM with proper chirality, showing the valley is a controllable DoF for light manipulation. Nontrivial topology and topological phase transition are also characterized with the nonzero valley Chern number. Valley-dependent edge states and the associated broadband robust transport are found at the edge of two topologically distinct VPCs. Compared with the electronic systems, the proposed VPC serves as a platform to explore analogous quantum physics due to its macroscopic nature; e.g., the bandwidth of a nontrivial band gap can be flexibly tuned, and the domain wall between two distinct VPCs can be readily designed (as elaborated upon in Figs. 3 and 4). Also compared to photonic topological insulators that break time-reversal symmetry, the valley-Hall type topological insulators are more straightforward to realize as only the inversion symmetry breaking is required. These advantages result in potential applications in nanophotonic systems, e.g., a photonic crystal slab and on-chip silicon-on-insulator platform. Our work has potential in the discovery of alternative topological states and the manipulation of spin-orbit interaction of light in nanophotonics.

[1] D. Xiao, W. Yao, and Q. Niu, Valley-Contrasting Physics in Graphene: Magnetic Moment and Topological Transport, Phys. Rev. Lett. **99**, 236809 (2007).

[2] A. Rycerz, J. Tworzydło, and C. W. J. Beenakker, Valley filter and valley valve in graphene, Nat. Phys. **3**, 172 (2007).

[3] H. Pan, Z. Li, C.-C. Liu, G. Zhu, Z. Qiao, and Y. Yao, Valley-Polarized Quantum Anomalous Hall Effect in Silicene, Phys. Rev. Lett. **112**, 106802 (2014).

[4] K. F. Mak, K. L. McGill, J. Park, and P. L. McEuen, The valley Hall effect in MoS_2 transistors, Science **344**, 1489 (2014).

[5] Z. Ye, T. Cao, K. O'Brien, H. Zhu, X. Yin, Y. Wang, S. G. Louie, and X. Zhang, Probing excitonic dark states in single-layer tungsten disulphide, Nature **513**, 214 (2014).

[6] Y. D. Lensky, J. C. W. Song, P. Samutpraphoot, and L. S. Levitov, Topological Valley Currents in Gapped Dirac Materials, Phys. Rev. Lett. **114**, 256601 (2015).

[7] M. Tahir and U. Schwingenschlögl, Valley polarized quantum Hall effect and topological insulator phase transitions in silicene, Sci. Rep. **3**, 1075 (2013).

[8] W. Yao, D. Xiao, and Q. Niu, Valley-dependent optoelectronics from inversion symmetry breaking, Phys. Rev. B **77**, 235406 (2008).

[9] G. Aivazian, Z. Gong, A. M. Jones, R.-L. Chu, J. Yan, D. G. Mandrus, C. Zhang, D. Cobden, W. Yao, and X. Xu, Magnetic control of valley pseudospin in monolayer WSe2, Nat. Phys. **11**, 148 (2015).

[10] A. Srivastava, M. Sidler, A. V. Allain, D. S. Lembke, A. Kis, and A. Imamoglu, Valley Zeeman effect in elementary opticalexcitations of monolayer WSe2, Nat. Phys. **11**, 141 (2015).

[11] X. Xu, W. Yao, D. Xiao, and T. F. Heinz, Spin and pseudospins in layered transition metal dichalcogenides, Nat. Phys. **10**, 343 (2014).

[12] T. Ma and G. Shvets, All-Si valley-Hall photonic topological insulator, New J. Phys. **18**, 025012 (2016).

[13] M. Padgett, J. Courtial, and L. Allen, Light's orbital angular momentum, Phys. Today **57**, 35 (2004).

[14] S. Franke-Arnold, L. Allen, and M. Padgett, Advances in optical angular momentum, Laser Photonics Rev. **2**, 299 (2008).

[15] X. Cai, J. Wang, M. J. Strain, B. Johnson-Morris, J. Zhu, M. Sorel, J. L. O'Brien, M. G. Thompson, and S. Yu, Integrated compact optical vortex beam emitters, Science **338**, 363 (2012).

[16] J. Lin, J. P. B. Mueller, Q. Wang, G. Yuan, N. Antoniou, X.-C. Yuan, and F. Capasso, Polarization-controlled tunable directional coupling of surface plasmon polaritons, Science **340**, 331 (2013).

[17] A. B. Young, A. C. T. Thijssen, D. M. Beggs, P. Androvitsaneas, L. Kuipers, J. G. Rarity, S. Hughes, and R. Oulton, Polarization Engineering in Photonic Crystal Waveguides for Spin-Photon Entanglers, Phys. Rev. Lett. **115**, 153901 (2015).

[18] M. Burresi, R. J. P. Engelen, A. Opheij, D. van Oosten, D. Mori, T. Baba, and L. Kuipers, Observation of Polarization Singularities at the Nanoscale, Phys. Rev. Lett. **102**, 033902 (2009).

[19] I. Söllner, S. Mahmoodian, S. L. Hansen, L. Midolo, A. Javadi, G. Kiršanskė, T. Pregnolato, H. El-Ella, E. H. Lee, J. D. Song, S. Stobbe, and P. Lodahl, Deterministic photon-emitter coupling in chiral photonic circuits, Nat. Nanotechnol. **10**, 775 (2015).

[20] J. Petersen, J. Volz, and A. Rauschenbeutel, Chiral nanophotonic waveguide interface based on spin-orbit interaction of light, Science **346**, 67 (2014).

[21] J. Lu, C. Qiu, M. Ke, and Z. Liu, Valley Vortex States in Sonic Crystals, Phys. Rev. Lett. **116**, 093901 (2016).

[22] D. Song, V. Paltoglou, S. Liu, Y. Zhu, D. Gallardo, L. Tang, J. Xu, M. Ablowitz, N. K. Efremidis, and Z. Chen, Unveiling pseudospin and angular momentum in photonic graphene, Nat. Commun. **6**, 6272 (2015).

[23] F. D. M. Haldane and S. Raghu, Possible Realization of Directional Optical Waveguides in Photonic Crystals with Broken Time-Reversal Symmetry, Phys. Rev. Lett. **100**, 013904 (2008).

[24] X. Ao, Z. Lin, and C. T. Chan, One-way edge mode in a magneto-optical honeycomb photonic crystal, Phys. Rev. B **80**, 033105 (2009).

[25] M. C. Rechtsman, J. M. Zeuner, Y. Plotnik, Y. Lumer, D. Podolsky, F. Dreisow, S. Nolte, M. Segev, and A. Szameit, Photonic Floquet topological insulators, Nature **496**, 196 (2013).

[26] A. B. Khanikaev, S. H. Mousavi, W.-K. Tse, M. Kargarian, A. H. MacDonald, and G. Shvets, Photonic topological insulators, Nat. Mater. **12**, 233 (2012).

[27] W. J. Chen, S. J. Jiang, X. D. Chen, B. Zhu, L. Zhou, J. W. Dong, and C. T. Chan, Experimental realization of photonic topological insulator in a uniaxial metacrystal waveguide, Nat. Commun. **5**, 5782 (2014).

[28] X.-D. Chen, Z.-L. Deng, W.-J. Chen, J.-R. Wang, and J.-W. Dong, Manipulating pseudospin-polarized state of light in dispersion-immune photonic topological metacrystals, Phys. Rev. B **92**, 014210 (2015).

[29] J.-W. Dong, X.-D. Chen, H. Zhu, Y. Wang, and X. Zhang, Valley photonic crystals for control of spin and topology, Nat. Mater. **16**, 298 (2017).

[30] D. L. Andrews and M. Babiker, *The Angular Momentum of Light* (Cambridge University Press, Cambridge, 2012).

[31] See Supplemental Material at http://link.aps.org/supplemental/10.1103/PhysRevB.96.020202 for details of (A) the correspondence between chiral OAM and circular polarized SAM, (B) valley-contrasting physics in photonic crystal slab, (C) detailed field distributions when bulk valley chiral states are excited, (D) the derivation of photonic effective Hamiltonian, (E) the numerical calculation of Berry curvature, and (F) the low transmission of W1 edge based Z-shape bend.

[32] S. Barik, H. Miyake, W. DeGottardi, E. Waks, and M. Hafezi, Two-dimensionally confined topological edge states in photonic crystals, New J. Phys. **18**, 113013 (2016).

[33] M. J. Collins, F. Zhang, R. Bojko, L. Chrostowski, and M. C. Rechtsman, Integrated optical Dirac physics via inversion symmetry breaking, Phys. Rev. A **94**, 063827 (2016).

[34] J.-L. Liu, W.-M. Ye, and S. Zhang, Pseudospin-induced chirality with staggered optical graphene, Light: Sci. Appl. **5**, e16094 (2016).

[35] L.-H. Wu and X. Hu, Scheme for Achieving a Topological Photonic Crystal by Using Dielectric Material, Phys. Rev. Lett. **114**, 223901 (2015).

[36] S. A. Skirlo, L. Lu, and M. Soljačić, Multimode One-Way Waveguides of Large Chern Numbers, Phys. Rev. Lett. **113**, 113904 (2014).

[37] W. Y. He and C. T. Chan, The emergence of Dirac points in photonic crystals with mirror symmetry, Sci. Rep. **5**, 8186 (2015).

[38] J. D. Joannopoulos, P. R. Villeneuve, and S. Fan, Photonic crystals: putting a new twist on light, Nature **386**, 143 (1997).

[39] A. H. P. I. Borel, L. H. Frandsen, and M. Kristensen, Topology optimization and fabrication of photonic crystal structures, Opt. Express **12**, 1996 (2004).